Research Article Vol. 33, No. 8 / 21 Apr 2025 / Optics Express 16778

Optics EXPRESS

# Integrated dispersion compensator based on cascaded silicon micro-ring resonators

ZHANQIANG HUI,[1,*] BIYING XIAN,[1] DONGDONG HAN,[1] TIANTIAN LI,[1] AND ABDEL-HAMID SOLIMAN[2]

[1] *School of Electronic Engineering, Xi'an University of Posts and Telecommunications, Xi'an 710121, China*
[2] *University of Staffordshire, Staffordshire ST4 2DE, UK*
[*] *zhanqianghui@xupt.edu.cn*

**Abstract:** Integrated dispersion management holds the key to enabling a diverse range of on-chip ultrafast all-optical signal processing operations in large-scale photonic integrated circuits (PICs). Here, a novel integrated silicon dispersion compensator based on cascading two dual-layer nested micro-ring resonators (MRRs) boasting an impressively large negative dispersion value is proposed. The structure was optimized by employing the finite-difference time-domain (FDTD) method. The numerical results reveal that the maximum group delay and negative dispersion of 266.41 ps and-34611.6 ps/nm, as well as -112.13 ps and -7567.1 ps/nm, were obtained at 1550 nm and 1545 nm, respectively. Meanwhile, the insertion loss (IL) of the device remains below 0.44 dB, and its footprint is only 25 μm × 27 μm. Additionally, the cumulative chromatic dispersion accrued by 40 Gbit/s on-off keying (OOK) signals, following their passage through 100 km of single-mode fiber (SMF), was successfully compensated. The consequent results validate the outstanding performance of the proposed dispersion compensator. The designed device is superior to previously reported results in terms of dispersion and footprint, and shows seamless compatibility with complementary metal-oxide-semiconductor (CMOS) technology, thus harboring great application potential in ultra-high-speed silicon photonic transceiver chips and related fields.



## 1. Introduction

Chromatic dispersion represents one of the crucial physical characteristic parameters of optical fibers. It stems from the phenomenon that light with diverse frequencies travels at different speeds within the optical fibers. In the domain of an optical fiber communication system, chromatic dispersion typically leads to the broadening of optical pulses. This pulse expansion, in turn, gives rise to inter-symbol interference (ISI), which adversely impacts the transmission quality of optical signals and undermines the overall performance of the optical fiber communication system [1]. With the exponential growth of the data transmission rate and the continuous extension of the transmission distance in current optical fiber communication systems, the impact of dispersion has become increasingly prominent. This makes it difficult to accurately recover the optical signal at the receiving end, thus increasing the system bit error rate (BER) and limiting the further improvement of the transmission rate and distance of the optical fiber communication system [2]. An effective solution to eliminate the impact of dispersion on the performance of optical fiber communication systems is to employ dispersion compensation techniques, which means introducing an optical device with negative dispersion into the fiber link to offset the accumulated positive dispersion in the original link [3]. Currently, the three most widely used dispersion compensators in commercial optical fiber networks are dispersion compensating fiber (DCF) [4], fiber Bragg grating (FBG) [5,6], and electronical dispersion compensation (EDC) [7,8]. Among them, the DCF scheme offsets the positive dispersion accumulated in the transmission fiber by introducing a section of dispersion compensating fiber with negative dispersion into the fiber link. This method can achieve a relatively large dispersion compensation, but it will increase

#554967 https://doi.org/10.1364/OE.554967
Journal © 2025 Received 6 Jan 2025; revised 14 Mar 2025; accepted 18 Mar 2025; published 7 Apr 2025

the transmission loss and complexity of the system. By contrast, the FBG scheme is based on the filtering characteristics of FBG. By reflecting the light of a specific wavelength, a delay is generated for the light of this wavelength, thus compensating for the dispersion. This scheme has a low insertion loss (IL) and a high dispersion compensation ability. Nevertheless, FBG is very sensitive to temperature changes. Slight temperature drift will cause the reflection wavelength to shift, thus affecting the dispersion compensation effect. Therefore, additional temperature control measures are generally required to stabilize its performance. Different from the previous two schemes, the EDC first converts the received optical signal into an electrical signal at the receiving end, and then processes the electrical signal in real-time by using digital signal processing (DSP) technology to eliminate the inter-symbol interference caused by dispersion. This method does not need to change the original fiber link, but it will increase the electrical complexity and power consumption of the system.

Recently, silicon-based integrated photonic devices have attracted significant attention owing to their advantages such as low power consumption, high integration density, and large bandwidth. The integrated photonic devices are capable of directly processing optical signals on the chip, which reduces the system size and cuts down the power consumption [9]. Moreover, the silicon-on-insulator (SOI) based on-chip photonic devices are compatible with complementary metal-oxide-semiconductor (CMOS) processes and offer tremendous application potential in high-energy consumption scenarios like future large-scale data centers, optical neural networks, and 5 G/6 G networks [10]. Up to now, various on-chip photonic devices, including on-chip all-optical wavelength converters [11], all-optical quantizers [12], all-optical logic gates [13], integrated optical frequency combs [14], quantum optical chips [15], silicon-based lasers [16], and mode-division multiplexers [17], have been reported. In 2024, Shekhar reported a high-performance silicon photonic transceiver chip. Nearly 60 active and passive photonic devices with functions such as optical emission, modulation, and reception were integrated within an area of less than 50 $mm^2$, achieving the transmission of 400Gb/s signals over 240 km [18]. Thanks to the advantages such as high speed, low cost, small size, and low power consumption, photonic chips have played a significant role in increasing the data transmission rate, reducing power consumption, and saving costs. They can be widely applied in optical fiber transmission networks, data centers, and high-performance computing equipment [19].

It is widely recognized that optical signals, before reaching the optical receiver, commonly undergo long-distance optical fiber link transmissions, wherein a considerable amount of dispersion accrues. As a result, dispersion compensation becomes indispensable before photoelectric conversion. Therefore, should an SOI-based dispersion compensation unit be successfully devised and subsequently employed to fabricate a high-speed optical transceiver chip endowed with dispersion compensation capabilities, it would possess outstanding scientific import and extensive engineering application prospects. Nonetheless, the extant research on on-chip dispersion compensators remains relatively scant. The current methodologies predominantly encompass schemes predicated on hybrid strip-slot optical waveguides [20], waveguide array gratings [21], waveguide Bragg gratings (WBG) [22,23], chirped multimode waveguide gratings (CMWGs) [24] and photonic crystal waveguides [25]. When these photonic devices are utilized as dispersion compensators, their dimensions typically span from several hundred μm to a few mm. Such dimensions continue to circumscribe their application within large-scale photonic integrated circuits (PICs). In the past two decades, micro-ring resonators (MRRs) have emerged as fundamental building blocks in integrated photonics. With advantages like compact size, low insertion loss, and high Q-value, they are widely used in constructing various functional photonic devices/chips, such as microwave generators [26], microwave photonic filters [27], tunable optical delay lines [28], optical frequency combs [29], photonic convolutional neural network chips [30], entangled photon pair generation [31] and on-chip photonic turnkey quantum source [32]. In 2013, Raktim Haldar established a theory of off-axis MRRs with single and multiple off-axis rings. Through numerical simulations combining the transfer matrix method and the finite difference time domain method, they found that, compared with the serially coupled conventional MRRs, off-axis MRRs perform better in terms of device size, faster response speed, and low dispersion [33]. Subsequently, they verified the performance of silicon-on-insulator (SOI) off-axis MRRs as electro-optic modulators (EOMs). The research results indicate that the additional single off-axis inner ring can effectively compensate for the thermal effects of the EOM. Notably, this structure is highly suitable for realizing high-speed dense wavelength division multiplexing optical communication systems in an extremely compact device size [34]. In 2016, M. Souza et al. utilized the temporal coupled - mode theory to analyze a nested or inner - coupled system composed of three MRRs. They demonstrated dispersion engineering and customized frequency responses, and predicted the existence of a dark state in this coupled system [35]. In 2018, Haldar further investigated the manufacturing tolerance of non - concentric nested MRRs (NN - MRRs). The results showed that when the sidewalls of the strip optical waveguides are either smooth or rough, the NN - MRR structure can relax the requirements for the critical coupling condition of MRRs by 20% [36]. Recently, dispersion compensators founded on micro-ring resonators (MRRs) have been put forward. In 2020, Vito. S et al. proposed a dispersion compensator composed of three all-pass MRRs. It accomplished the compensation for the dispersion amassed during the 30 km transmission of 100 Gb/s PolMux-NRZ signals with a central wavelength of 1550 nm in a single-mode fiber [37]. In 2022, Liu et al. introduced a continuously tunable dispersion compensator predicated on cascaded MRRs. By concatenating seven micro-rings of varying diameters, this compensator achieved a maximum dispersion value of -720 ps/nm, empowering it to offset the dispersion generated by a single-mode fiber of up to 40 km in length. The device measured 3.8 mm by 0.3 mm [38]. In the same year, K. Y. K. Ong et al. proposed a tunable dispersion compensator based on an add-drop MRR, attaining a dispersion range from $+12.9 \times 10^3$ ps/nm to $-12.3 \times 10^3$ ps/nm. After compensation by this device, the BER of 25 Gbit/s NRZ data transmitted over 20 km of single-mode fiber diminished from $10^{-3}$ to $10^{-11}$, markedly augmenting the signal quality [39]. Although the aforementioned devices have achieved certain feats in on-chip dispersion compensation, with the rapid acceleration of the rate in optical fiber communication systems, the incessant elongation of the transmission distance, and the expeditious growth of the rate of silicon photonic transceiver chips, there is an acute and exigent need for on-chip dispersion compensators with greater dispersion magnitudes and enhanced levels of integration.

In this work, a novel cascaded nested micro-ring dispersion compensator based on SOI with an extremely high negative dispersion value was proposed. By cascading two dual-layer nested micro-rings of different sizes, this device achieves a large group delay and an extremely high negative dispersion. The simulation results show that the proposed dispersion compensator has dual operating wavelengths. At 1550 nm, the maximum group delay is 266.41 ps, and the largest negative dispersion is -34611.6 ps/nm. At 1545 nm, the maximum group delay is -112.13 ps, and the largest negative dispersion is -7567.1 ps/nm. Meanwhile, the device size is only $25\,\mu m \times 27\,\mu m$, and the IL is less than 0.44 dB. After dispersion compensation using this device, the BER of the 40 Gbit/s NRZ data signals at 1550.04 nm and 1545.12 nm, after transmission through 100 km of single-mode fiber (SMF), are reduced to $10^{-15}$ and $10^{-13}$, respectively, with a significant improvement in the eye diagram. The proposed on-chip dispersion compensator is compatible with CMOS technology, has a small footprint, and is convenient for large-scale integration, demonstrating great application potential in high-performance photonic transceiver chips and large-scale PICs.

## 2. Structure design and optimization

The structure of the proposed cascaded nested micro-ring dispersion compensator is shown in Fig. 1. The blue part represents the silica substrate, while the red part denotes the silicon core

Optics EXPRESS

layer, and the upper cladding layer of the waveguide is silica. The structure consists of a straight waveguide and four micro-rings with different radii, where two nested micro-rings are cascaded via the straight waveguide. In Fig. 1, the optical signal enters through the input port of the straight waveguide, is subject to dispersion compensation, and is then output through the output port. All waveguides are strip waveguides, with the width and height being $W$ and $H$, respectively. The radius of the large ring in the first nested micro-ring is denoted as $R_1$, and the radius of the small ring is $R_2$. In the second nested micro-ring, the radius of the large and small rings is denoted as $R_3$ and $R_4$, respectively. The distance between the straight waveguide and the large ring, as well as between the large ring and the small ring are both $g$. The distance between the centers of the first and second nested rings along the x-axis is denoted by $G$. Since the resonance wavelength of a single MRR is closely related to the group refractive index (i.e., different wavelengths of light travel at different speeds when passing through the micro-ring), the group velocity characteristics of the micro-ring can be controlled by adjusting the structural parameters of the micro-ring (such as the radius, coupling coefficient, etc.) or by selecting different waveguide materials, so as to compensate or regulate the dispersion. The material models for silica and silicon are determined by their Sellmeier equations [40].

$$n^2(\lambda) = 1 + \sum_{i=1}^{k} \frac{B_i \lambda^2}{\lambda^2 - C_i} \tag{1}$$

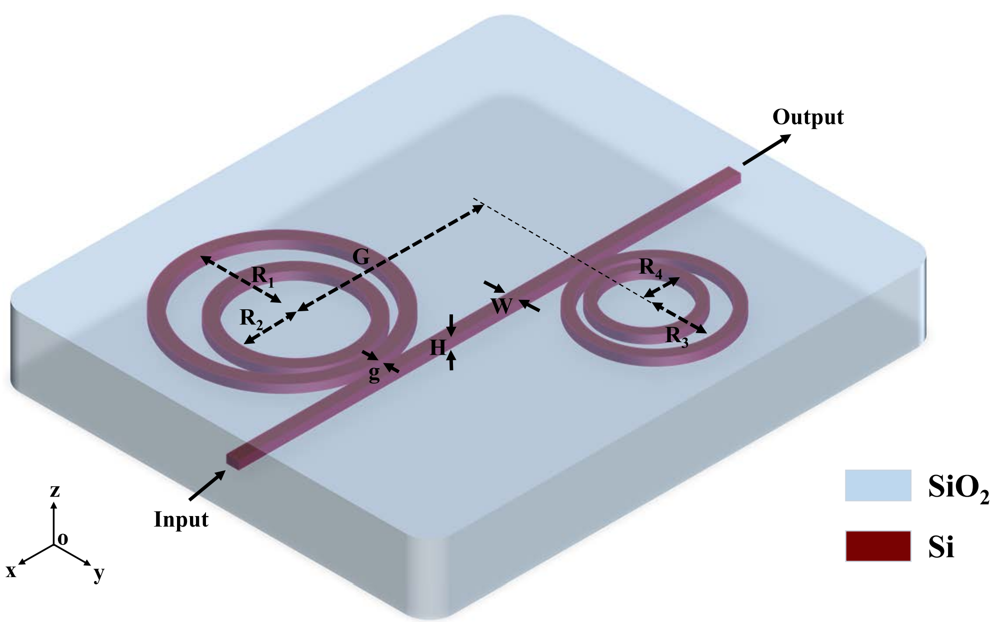


**Fig. 1.** Schematic of the cascaded nested micro-ring structure.

In the above equation, $\lambda$ represents the incident wavelength, measured in micrometers; $B_i$ are the Sellmeier coefficients, which are typically constant terms; $C_i$ is the Sellmeier dispersion constants, which generally represent the square values of the material's resonance wavelengths, with units in $\mu m^2$; typically, $k$ is taken as 3. For silica, the specific parameters in the Sellmeier equation are: $B_1 = 0.6961663$, $B_2 = 0.4079426$, $B_3 = 0.8974794$, $C_1 = 0.00467914$, $C_2 = 0.0135120$, and $C_3 = 97.934$. For silicon, $B_1 = 10.6684293$, $B_2 = 0.0030434748$, $B_3 = 1.54133408$, $C_1 = 0.301516485$, $C_2 = 1.13475115$, and $C_3 = 1104$.

The mode characteristics of the strip straight waveguide in the proposed structure are analyzed using the Finite Difference Eigenmode (FDE) solver in Ansys Lumerical MODE Solutions. To avoid intermodal crosstalk, the waveguide is designed as a single-mode strip waveguide. Meanwhile, to reduce the transmission loss of the waveguide, the waveguide dimensions are set as $W = 600$ nm and $H = 220$ nm. Simulation results indicate that this strip waveguide only supports the $TE_0$ mode, and its electric field distribution is shown in Fig. 2(a). It can be observed that the energy is well confined within the waveguide core. Moreover, the effective refractive index of the $TE_0$ mode in the optical waveguide is a key parameter, which will influence the optical characteristics, including the resonant wavelength and transmittance of the MRR. The variation of the effective refractive index of the $TE_0$ mode in this optical waveguide with the operating wavelength is shown in Fig. 2(b). As seen, the effective refractive index of the $TE_0$ mode in the straight waveguide is approximately 2.566 at the operating wavelength of 1550 nm.

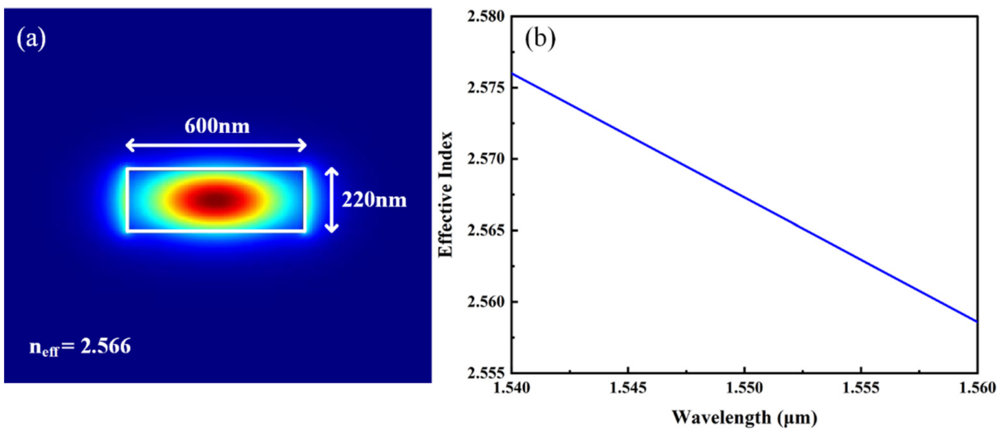


**Fig. 2.** (a) Mode profile of the straight waveguide at 1550 nm. (b) The variation of the effective refractive index with wavelength.

For a single micro-ring, when light propagates through one circumference of the micro-ring and the resulting phase shift is 2π, the micro-ring will be in a resonant state. The resonance condition of the micro-ring can be expressed as follows [41]:

$$\lambda_{\text{res}} = \frac{n_{\text{eff}} L}{m}, \quad m = 1, 2, 3 \ldots \tag{2}$$

here, $\lambda_{\text{res}}$ is the resonant wavelength, $n_{\text{eff}}$ is the effective refractive index of the guided mode supported by the optical waveguide, $L$ is the circumference of the micro-ring, and $m$ is the resonance order. According to Eq. (2), we first set the resonant wavelength at 1550 nm, which is the center wavelength of the C - band in optical fiber communication. Meanwhile, considering the precision of the existing CMOS technology and referring to the initial structure of the MRRs reported in previous literature [42], the resonant orders of the four micro-rings in the designed cascaded MRRs were determined respectively, that is $m_1 = 80$, $m_2 = 40$, $m_3 = 40$, and $m_4 = 20$, respectively, and the corresponding radii were also obtained. Then, according to the relevant empirical on the influence of the coupling distance on the coupling efficiency in silicon-based MRRs, the structural parameters such as the size of the micro-rings and the coupling spacing were scanned from small to large, and numerical simulations were carried out for each set of parameters. Finally, the initial radii of the four micro-rings were roughly determined to be around $R_1 = 6.706$μm, $R_2 = 4.785$μm, $R_3 = 4.792$μm, $R_4 = 2.982$μm, and $G = 10$μm. Nevertheless, at this time, the total dispersion of the proposed cascaded nested MRRs-based dispersion compensator is still small, and efficient dispersion compensation cannot be achieved. To obtain a higher total dispersion value, we need to optimize each structural parameter one by one using the control - variable method, to achieve a large group delay and acquire the maximum negative dispersion. In the following optimization process, we will use the Finite-Difference Time-Domain (FDTD) solver in the Ansys Lumerical photonic simulation software.

Group delay is an important parameter for micro-ring-based dispersion compensators. The group delay in the MRR reflects the propagation delay of light wave within the micro-ring, and its value is closely related to the structural parameters of the micro-ring. It can be derived from the derivative of the phase concerning frequency. It is typically expressed as [43]:

$$\tau_g = \frac{d\phi(\omega)}{d\omega} = \frac{L}{c} \cdot \frac{dn_{\mathrm{eff}}(\omega)}{d\omega} + \frac{n_{\mathrm{eff}}(\omega) \cdot L}{c} \tag{3}$$

here, $\tau_g$ is the group delay, $\phi$ represents the phase shift generated after light propagates one full circumference around the micro-ring, $\omega$ is the optical frequency. $L$ is the circumference of the micro-ring, and $c$ is the speed of light.

Dispersion is typically expressed as the inverse of the derivative of group delay with respect to wavelength, i.e., [43]

$$D(\lambda) = \frac{\mathrm{d}\tau_g(\lambda)}{\mathrm{d}\lambda} \tag{4}$$

here, $D$ represents the dispersion, and $\lambda$ is the wavelength.

Based on the above analysis, the dispersion characteristics of micro-rings are closely related to their specific geometric structures. Therefore, for the designed cascaded nested micro-ring dispersion compensator, it is necessary to analyze the influence of structural parameters including the large ring radius $R_1$, the small ring radius $R_2$ in the first nested ring, the large ring radius $R_3$, the small ring radius $R_4$ in the second nested ring, and center-to-center distance $G$, on its group delay and dispersion one by one, with the expectation of obtaining the optimal dispersion compensator structure.

Firstly, the influence of the radius $R_1$ of the large ring in the first nested MRR on the dispersion and delay characteristics of the device was investigated. In the simulation, the radius $R_2$ of the small ring in the first nested ring was set as 4.795 µm, the radius $R_3$ of the large ring in the second nested ring was set as 4.802 µm, the radius $R_4$ of the small ring in the second nested ring was set as 3 µm, the coupling gap $g$ was set as 0.1 µm, and the distance $G$ between the centers of the two nested rings was set as 10 µm. $\mathrm{R}_1$ was increased from 6.706 µm to 6.726 µm with a step size of 0.005 µm. The dependency of the group delay and dispersion with the working wavelength are shown in Figs. 3(a) - (b) respectively. It can be observed that as $R_1$ increases, the wavelengths corresponding to the peak group delay in Fig. 3(a) and the peak dispersion in Fig. 3(b) gradually shift towards the red end of the optical spectrum. Meanwhile, the maximum group delay has changed from positive to negative. For $R_1 = 6.706$, 6.711, and 6.716 µm, the dispersion value jumps from anomalous dispersion to normal dispersion. For $R_1 = 6.721$, 6.726 µm, it jumps from normal dispersion to anomalous dispersion. The variation trend of the dispersion slope changes from positive-negative-positive to negative-positive-negative. When $R_1$ increases from 6.706 µm to 6.716 µm, the maximum value of the group delay increases from 20.41 ps to 179.38 ps, and the dispersion value decreases from -269.58 ps/nm to -16148.7 ps/nm. When $R_1$ increases from 6.716 µm to 6.726 µm, the maximum value of the group delay decreases from 179.38 ps to -28.86 ps, and the dispersion value increases from -16148.7 ps/nm to -1072.01 ps/nm. Thus, $R_1 = 6.716$ µm is selected as the optimal structural parameter for the large ring in the first nested ring.

Secondly, the impact of the small ring radius $R_2$ in the first nested MRR on the group delay and dispersion of the proposed structure is investigated. In the simulation, $R_1 = 6.716$ µm, $R_3 = 4.802$ µm, $R_4 = 3$ µm, $g = 0.1$ µm, and $G = 10$ µm. The value of $R_2$ is increased from 4.785 µm to 4.805 µm in a step size of 0.005 µm. The resulting group delay and dispersion as a function

Optics EXPRESS

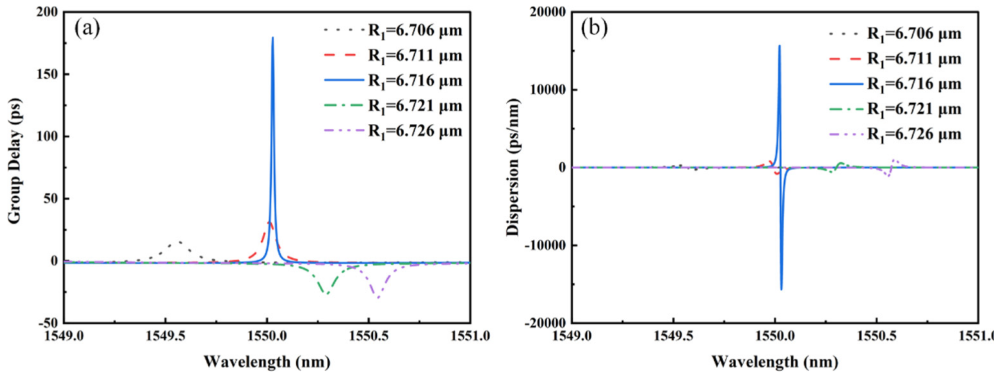


**Fig. 3.** (a) Variation of group delay with wavelength for different values of $R_1$. (b) Variation of dispersion with wavelength for different values of $R_1$.

of the operating wavelength are shown in Fig. 4(a) and (b), respectively. It can be observed that as $R_2$ increases, the peak wavelengths corresponding to both the group delay and negative dispersion gradually redshift. The peak group delay has changed from negative to positive, and the variation trend of the dispersion slope has changed from negative-positive-negative to positive-negative-positive. Compared to Fig. 2, the influence of $R_2$ on the operating wavelength is less pronounced than that of $R_1$. For the five selected values of $R_2$, the corresponding dispersion extrema wavelengths are all within the range of 1550 nm to 1550.05 nm. When $R_2$ increases from 4.785 µm to 4.795 µm, the peak values of the group delay are -32.9 ps, -67.53 ps, and 179.38 ps, and the peak values of dispersion are -491.34 ps/nm, -2203.15 ps/nm, and -16148.7 ps/nm. When $R_2$ increases from 4.795 µm to 4.805 µm, the peak group delay decreases from 179.38 ps to 17.11 ps, and the peak negative dispersion increases from -16148.7 ps/nm to -180.67 ps/nm. Based on these results, a value of $R_2 = 4.795$ µm is chosen for the small ring radius in the first nested ring.

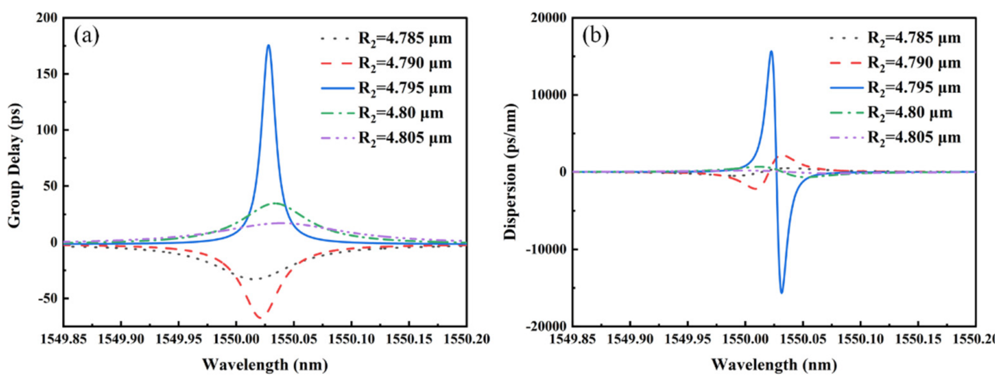


**Fig. 4.** (a) Variation of group delay with wavelength for different values of $R_2$; (b) variation of dispersion with wavelength for different values of $R_2$.

Next, the influence of the outer ring radius $R_3$ of the second nested MRR on the group delay and dispersion of the proposed structure is investigated. In this simulation, $R_3$ is increased from 4.792 µm to 4.812 µm with a step size of 0.005 µm, while keeping other structural parameters constant. The results are shown in Fig. 5. As can be seen from Fig. 5(a), with the increase of $R_3$, the peak values of group delay corresponding to the five $R_3$ values are -41.19 ps, 67.29 ps, 179.38 ps, 76.72 ps, and 43.2 ps, respectively. In Fig. 5(b), the corresponding peak values of dispersion for the five $R_3$ values are -935.72 ps/nm, -2560.08 ps/nm, -16148.7 ps/nm, -3434.84

ps/nm, and -1026.61 ps/nm, respectively. Only when $R_3 = 4.792\mu m$, the corresponding group delay is negative, and the dispersion slope shows a trend of negative-positive-negative. For the other values of $R_3$, the corresponding group delays are all positive, and the dispersion slope presents a variation trend of positive-negative-positive. Thus, $R_3 = 4.802\,\mu m$ is selected.

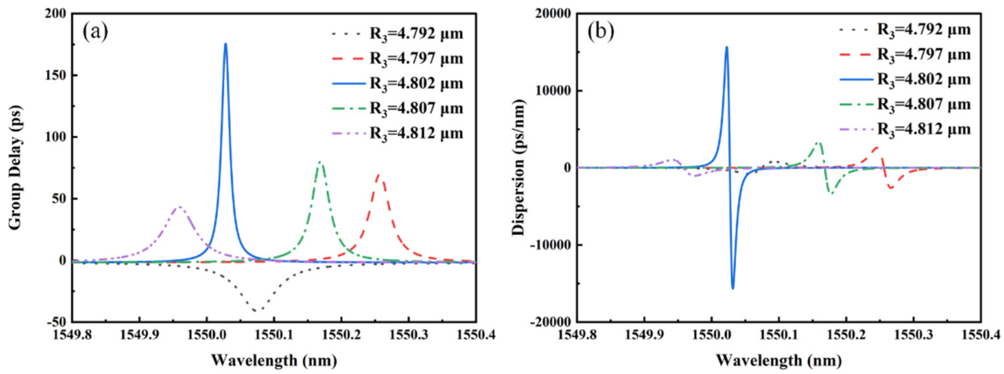


**Fig. 5.** (a) Variation of group delay with wavelength for different $R_3$. (b) Variation of dispersion with wavelength for different $R_3$.

Furthermore, the influence of the inner radius $R_4$ of the second nested MRR on the group delay and dispersion is investigated. In this analysis, $R_4$ is gradually increased from 2.982 μm to 3.002 μm in a step size of 0.005 μm, while other parameters are constant. The results are shown in Fig. 6. As seen in Fig. 6(a), the wavelength corresponding to the peak group delay gradually redshifts with the increase of $R_4$, with each step increase in $R_4$ resulting in a redshift of approximately 0.02 nm. Figure 6(b) shows that the peak dispersion value first decreases and then increases with the increase of $R_4$. Specifically, when $R_4$ increases from 2.982 μm to 2.992 μm, the peak of group delay increases from 179.375 ps to 266.41 ps, and the peak dispersion value decreases from -15605.4 ps/nm to -34611.6 ps/nm. When $R_4$ increases from 2.992 μm to 3.002 μm, the peak of group delay decreases from 266.41 ps to 218.38 ps, and the peak dispersion value increases from -34611.6 ps/nm to -22150.4 ps/nm. It can be learned that for all values of $R_4$, the group delay is positive, and the dispersion slope shows a trend of positive-negative-positive. Based on the above analysis, $R_4 = 2.992\,\mu m$ is selected.

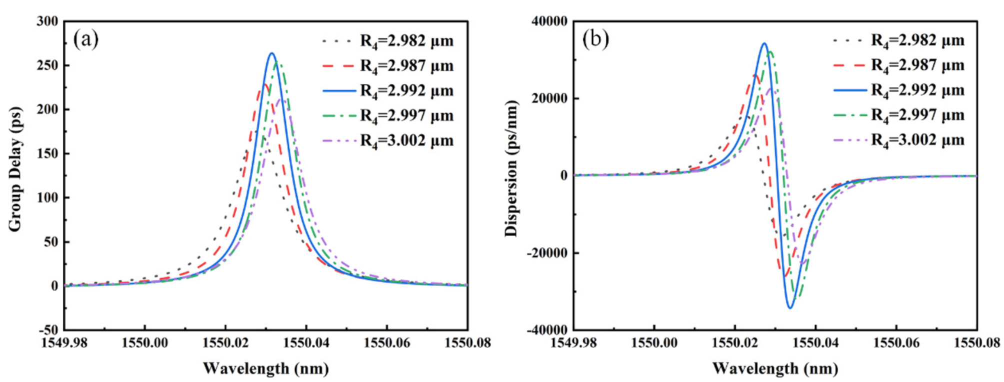


**Fig. 6.** (a) Variation of group delay with wavelength for different $R_4$. (b) Variation of dispersion with wavelength for different $R_4$.

Finally, the impact of the center-to-center distance $G$ between the left and right nested MRRs on the group delay and dispersion of the proposed cascaded nested micro-ring dispersion compensator is investigated. In the numerical analysis, $G$ is increased from 9.8 μm to 10.2 μm in a step size of 0.1 μm, while the other structural parameters remain unchanged. The results are shown in Fig. 7. As observed from the figure, when $G$ increases from 9.8 μm to 10 μm, the wavelengths corresponding to the peak group delay and peak dispersion gradually approach 1550 nm, while the peak group delay increases from -27.81 ps to 266.41 ps, and the peak dispersion value decreases from -26.8 ps/nm to -34611.6 ps/nm. When $G$ increases from 10 μm to 10.2 μm, the wavelengths corresponding to the peaks group delay and peak dispersion gradually shift away from 1550 nm. Additionally, the peak group delay decreases from 266.41 ps to 19.14 ps, and the peak dispersion value increases from -34611.6 ps/nm to -217.3 ps/nm. Only when $G = 0.1$μm, the group delay corresponding to this structure is negative, and the variation trend of the dispersion slope is negative-positive-negative. In contrast, when $G$ takes other values, the group delays corresponding to this structure are all positive, and the dispersion slopes all show a variation trend of positive-negative-positive. Then, $G = 10$ μm is selected as the optimal center-to-center distance between the two nested MRRs.

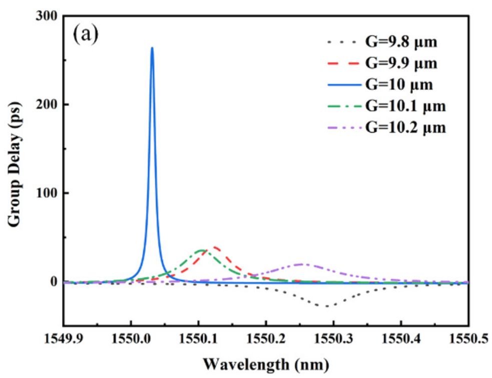


**Fig. 7.** (a) Variation of group delay with wavelength for different values of G; (b) variation of dispersion with wavelength for different values of G.

Based on the above analysis results, the optimal structural parameters for the cascaded nested MRRs are $W = 600$ nm, $H = 220$ nm, $g = 0.1$ μm, $R_1 = 6.716$ μm, $R_2 = 4.795$ μm, $R_3 = 4.802$ μm, $R_4 = 3$ μm, and $G = 10$ μm.

## 3. Performance analysis

For the optimized cascaded nested MRR dispersion compensator, numerical analysis was conducted on the relationship between its group delay and dispersion concerning wavelength, and the results are shown in Fig. 8. The blue curve represents the group delay, while the red curve denotes the dispersion. Specifically, as can be seen from Fig. 8(a), the device can achieve extremely large group delays and high dispersion values at two wavelengths. Among them, the group delay reaches a maximum value of 266.41 ps at a wavelength of 1550.032 nm, and the dispersion reaches its maximum value of -34611.6 ps/nm at a wavelength of 1550.034 nm. This indicates that at these wavelengths, the propagation speed of light waves within the nested MMR is significantly slowed down, implying that the transmission time of light in the resonant state is significantly increased. In addition, as shown in Fig. 8(b), another relatively large group delay and a high dispersion value near 1545 nm for this structure are observed. The group delay reaches a minimum value of -112.13 ps at a wavelength of 1545.13 nm, and the dispersion value reaches a minimum value of -7567.1 ps/nm at a wavelength of 1545.125 nm.

Next, the electric field distribution (X-O-Y plane) in the cascaded nested MRR dispersion compensator is analyzed, and the results are illustrated in Fig. 9(a). It can be observed that the

Optics EXPRESS

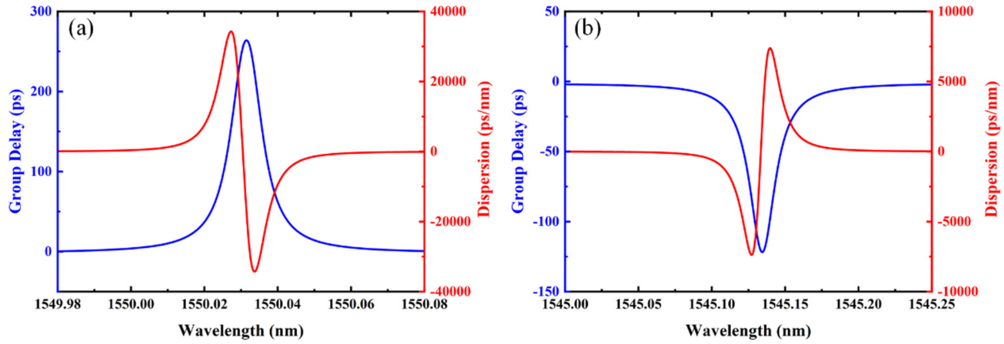


**Fig. 8.** (a) Group delay and dispersion versus wavelength near 1550 nm for the optimized structure. (b) Group delay and dispersion versus wavelength near 1545 nm for the optimized structure.

energy is higher in the large ring of the first nested MRR and the small ring of the second nested MRR, indicating an over-coupled state. Conversely, the energy is lower in the small ring of the first nested MRR and the large ring of the second nested MRR, indicating an under-coupled state. Figure 9(b) and Fig. 9(c) show the modal field distribution at the input and output ports, respectively, on the cross-sectional view (Y-O-Z plane). It can be observed that compared with the input end, when the optical wave reaches the output end after being transmitted through the cascaded nested MRRs, its mode field energy distribution remains nearly unchanged and is still in the $TE_0$ mode.

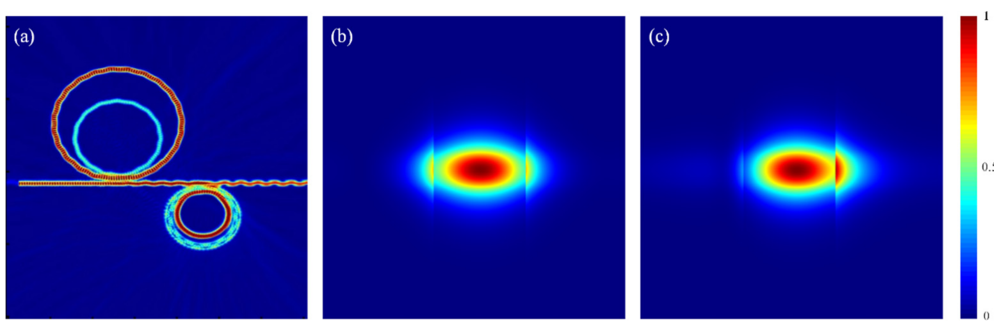


**Fig. 9.** (a) Electrical field distribution in the X-O-Y plane. Electrical field distribution at (b) the input port and (c) the output port of the straight waveguide.

For a single-ring MRR, its transmission spectrum T(ω) can be expressed as [38]:

$$T = \frac{t^2 + a^2 - 2ta\cos\phi}{1 - 2ta\cos\phi + (ta)^2} \tag{5}$$

here, k is the coupling coefficient between the input straight waveguide and the micro-ring, $t$ is the transmission coefficient, satisfying $|\mathrm{k}|^2 + |t|^2 = 1$; $a$ is the loss coefficient of the micro-ring, representing the loss of light after one round-trip propagation within the micro-ring; and $\phi$ is the phase shift induced by the light after one round-trip propagation within the micro-ring. Based on this, the transmission spectrum of the proposed cascaded nested MRRs is shown in Fig. 10. It can be observed that there are two minimum values in the transmission spectrum near 1545 nm and 1550 nm respectively, with the corresponding transmittances being -0.44 dB and -0.43 dB. This indicates that the designed cascaded nested MRRs are indeed in a detuned state at these two

Optics EXPRESS

wavelengths, which meets the conditions for generating large dispersion values. In addition, this figure also shows that the insertion loss of the designed device within the wavelength range of 1540 to 1560 nm is less than 0.44 dB, indicating that the cascaded nested MRRs-type dispersion compensator has the advantage of low insertion loss. It is worth noting that the insertion loss of the device obtained from the simulation in Fig. 10 only represents the insertion loss of the proposed integrated dispersion compensator itself. When integrating the designed device into an actual optical fiber communication link, the coupling loss from the fiber to the chip is a key issue that needs to be addressed [32]. The coupling loss between the optical fiber and the optical chip can be further reduced by fabricating tapered waveguides at the end - faces of the input and output straight waveguides of the dispersion compensation optical chip containing nested MRRs.

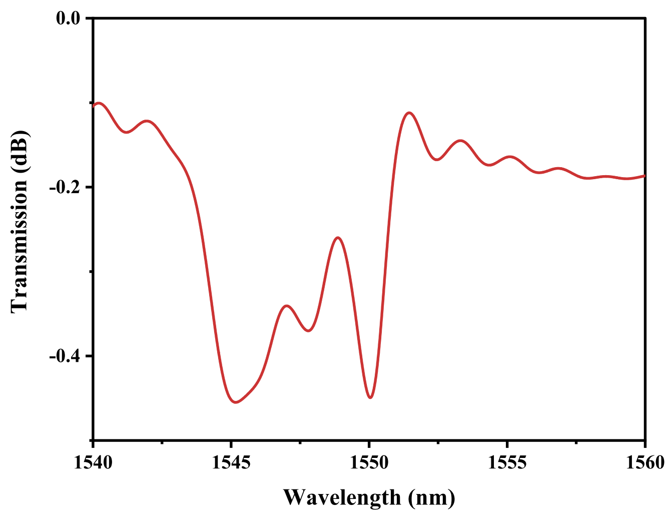


**Fig. 10.** Transmission spectrum of the cascaded MRRs.

The local zoomed-in transmission spectrum around 1550 nm and 1545 nm is compared with the corresponding group delay curves within the same wavelength range, as shown in Fig. 11. The red curve represents the transmission spectrum, and the blue curve represents the group delay. From Fig. 11(a), it can be seen that at the resonant wavelength of 1550 nm, the group delay reaches its peak value of 266.41 ps. Similarly, in Fig. 11(b), the group delay at the resonant wavelength of 1545 nm reaches its peak value of -112.13 ps.

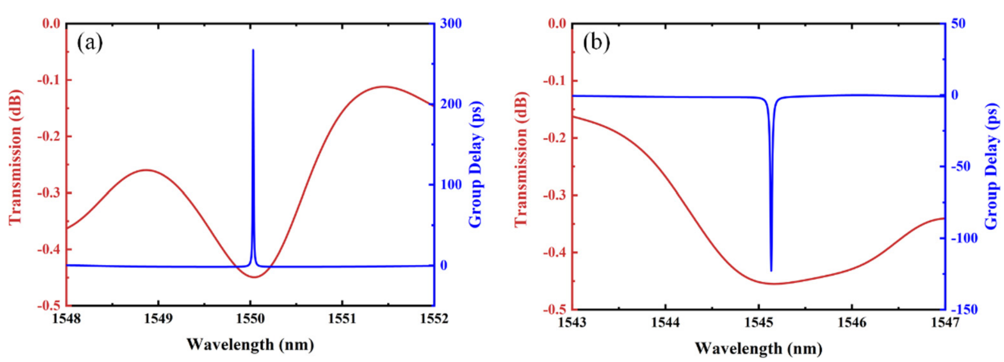


**Fig. 11.** Transmission spectrum and group delay as a function of wavelength (a) near 1550 nm and (b) near 1545 nm.

Optics EXPRESS

To verify the dispersion compensation effect of the designed cascaded nested MRR dispersion compensator, it was used to compensate for the dispersion of high-speed data transmitted through long-distance SMF. Considering that although coherent optical communication technology is widely adopted in current long-distance backbone networks, the intensity-modulation direct-detection (IMDD) scheme is still used in some special application scenarios with an optical fiber transmission distance exceeding 100 km, especially in fields such as military defense and national security. Take the underwater fiber-optic guided torpedo combat system as an example. It usually adopts the IMDD scheme [44]. After the torpedo is launched, the operators on the submarine can remotely guide the torpedo through the fiber-optic communication system to carry out long-range and precise strikes on targets 100 km away and even farther. In addition, in situations where secure communication is required, chaotic secure communication technology is often employed. In 2019, Fu et al. proposed and experimentally verified a new physical-layer encryption scheme for high-speed optical communication, achieving the secure transmission of a 10 Gbit/s on-off keying (OOK) signal in a 100-km standard single - mode fiber (SMF) [45]. Therefore, here, we used the commercially available optical fiber communication system simulation software OptiSystem to build an IMDD optical fiber communication system based on a 100 - km SMF, to evaluate the performance of the proposed integrated dispersion compensator. OptiSystem creates a system - level simulator, integrating functions such as designing, testing, and optimizing of various types of broadband optical networks [46]. It enjoys extremely high popularity in the field of optical fiber communication and is widely used for simulating various issues, including wavelength division multiplexing (WDM), optical time division multiplexing (OTDM), optical code division multiplexing (OCDMA), and coherent as well as IMDD optical communication systems [47–49]. Its accuracy has been unanimously recognized by numerous researchers from academia and industry. The specific dispersion compensation system is shown in Fig. 12. A pseudo - random bit sequence (PRBS) generator produces a 40 Gbit/s PRBS, which is injected into a non-return-to zero (NRZ) generator to generate a 40 Gbit/s NRZ signal. This signal is then injected into a Mach-Zehnder intensity modulator to perform intensity modulation on the continuous light injected into the modulator. A polarization controller (PC) is used to optimize the polarization state of the continuous light to ensure the optimal intensity modulation effect. The modulated optical signal passes through an erbium-doped optical fiber amplifier (EDFA) to amplify its optical power and is then injected into a 100 - km SMF for long - distance transmission. Since the SMF has an attenuation coefficient of 0.2 dB/km around 1550 nm, the optical power of the signal after long - distance transmission is relatively low. It is further amplified by another EDFA and then injected into the designed integrated dispersion compensator for dispersion compensation. The compensated optical signal is injected into a PIN photodetector for photoelectric conversion, then passes through a Bessel low - pass filter to filter out low - frequency electrical noise. Finally, an oscilloscope and a bit - error rate (BER) tester are used to monitor the waveform, eye diagram, and BER of the terminal signal. During the simulation, the selection of the central wavelength of the optical signal to be compensated is of critical importance. By referring to the group delay and dispersion curves (as depicted in Fig. 8), we deliberately avoid the peak of the group delay, because the dispersion is zero at this point. Given that a larger negative dispersion value leads to better dispersion compensation, we draw a dashed line at $D$ = - 9556 ps/nm in the vicinity of 1550 nm. This dashed line intersects with the dispersion curve, yielding two intersection points, as illustrated in Fig. 8(a). The corresponding wavelengths at these two points are 1550.031 nm and 1550.04 nm, respectively. According to the principle of dispersion compensation: $D_1L_1 = D_2L_2$, where $D_1$ and $L_1$ is the dispersion coefficient and length of the standard SMF at wavelength λ, $D_2$ and $L_2$ is the dispersion coefficient and length of the dispersion compensator at wavelength λ. Considering the dispersion coefficient of a SMF at 1550 nm is $D_1$ = 17 ps/nm/km, thus, if the central wavelength of the optical signal to be compensated is set within this wavelength range, it can ensure good dispersion compensation results. Similarly,

Optics EXPRESS

for the other operating channel, we draw a dashed line at $D$ = - 4613 ps/nm around 1545 nm. This line intersects with the dispersion curve, resulting in two intersection points (the corresponding wavelengths are 1545.12 nm and 1545.13 nm, respectively), as shown in Fig. 8(b). If the central wavelength of the optical signal to be compensated is set within this range, it can ensure good dispersion compensation results. Therefore, in the simulation system, a continuous wave laser with a central wavelength of 1550.04 nm or 1545.12 nm was selected.

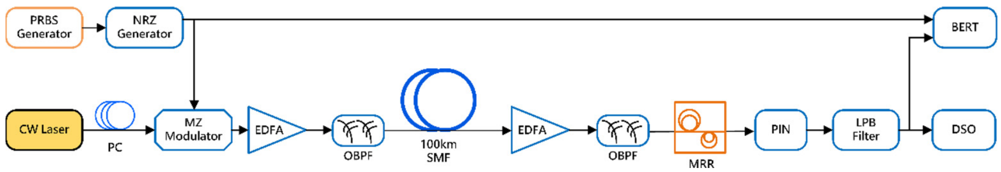


**Fig. 12.** Experimental setup of the dispersion compensation system.

As illustrated in Figs. 13(a) and 13(d), the waveform and eye diagram of the original signal with a wavelength of 1550.04 nm are presented respectively. Subsequently, Figs. 13(b) and 13(e) respectively depict the waveform and eye diagram of this optical signal following its transmission through 100 km of SMF. Moreover, Figs. 13(c) and 13(f) show the waveform and eye diagram of the signal after undergoing dispersion compensation. In a similar vein, Figs. 13(g) and 13(j) display the waveform and eye diagram of the original signal possessing a wavelength of 1545.12 nm, while Figs. 13(h) and 13(k) illustrate the waveform and eye diagram of the signal after its transmission through 100 km of SMF. Finally, Figs. 13(i) and 13(l) present the waveform and eye diagram of the signal after dispersion compensation. Evidently, for the optical signals with wavelengths of 1550.04 nm and 1545.12 nm, upon transmission through the long-distance SMF, the dispersion effect leads to a severe distortion of the optical signals, with the eye diagrams nearly closing. However, in comparison to the eye diagrams of the optical signals prior to compensation (as shown in Figs. 13(e) and 13(k)), the openings of the eye diagrams in Figs. 13(f) and 13(l) are noticeably enlarged. Concurrently, for the optical signal with a wavelength of 1550.04 nm, the Q factor after dispersion compensation reaches 7.71, and the minimum BER is $10^{-15}$. For the optical signal with a wavelength of 1545.12 nm, the Q factor after dispersion compensation is 7.18, and the minimum BER is $10^{-13}$. This demonstrates that after the dispersion compensation is carried out by the designed cascaded nested MRR dispersion compensator, the degree of signal distortion is remarkably reduced, and the performance of the optical fiber communication system is substantially enhanced. Hence, it verifies the outstanding dispersion compensation effect of the designed cascaded nested MRR dispersion compensator.

On the other hand, the current CMOS manufacturing process inevitably has limitations in controlling the dimensional accuracy of waveguides. This issue is particularly prominent for MRRs with high refractive index contrast, which can cause changes in the resonant wavelength. Meanwhile, in actual optical fiber communication systems, the light source may also experience frequency chirping or wavelength drift. Therefore, the operating wavelength of the dispersion compensator should have dynamic tuning capabilities. Tuning the resonant wavelength of the MRRs based on the electro-optic or thermo-optic effect are two viable solutions [50,51]. However, compared with the electro - optic effect, the thermo-optic effect in silicon waveguides is more significant, which allows the phase shifter to require a lower driving voltage. In addition, the thermo-optic effect does not have the DC drift phenomenon and can provide a more stable solution for phase tuning [51]. Therefore, for the integrated dispersion compensator proposed in this paper, dynamic tuning of the device's operating wavelength can be achieved through the thermo-optic effect by depositing nickel - chromium metal electrodes on the optical waveguide. The specific physical mechanism of thermo-optic tuning is as follows: when current is injected into the heater, the temperature of the optical waveguide will rise. Since silicon has a relatively

Optics EXPRESS

large positive thermoelectric coefficient, an increase in the temperature of the silicon waveguide leads to an increase in the waveguide's refractive index, which in turn causes a drift in the resonant wavelength of the MRRs, thus achieving the purpose of dynamically tuning the operating wavelength.

The main performance parameters of the proposed cascaded nested MRR dispersion compensator are compared with those of previously reported on-chip dispersion compensators, and the results are shown in Table 1. The typical parameters for comparison include device structure, dispersion value, IL, and device size, etc. It can be learned that for the structure reported in [39], although its IL is slightly smaller than that of the proposed structure in this work, its dispersion value is also smaller than our scheme. More importantly, its size is significantly larger than that

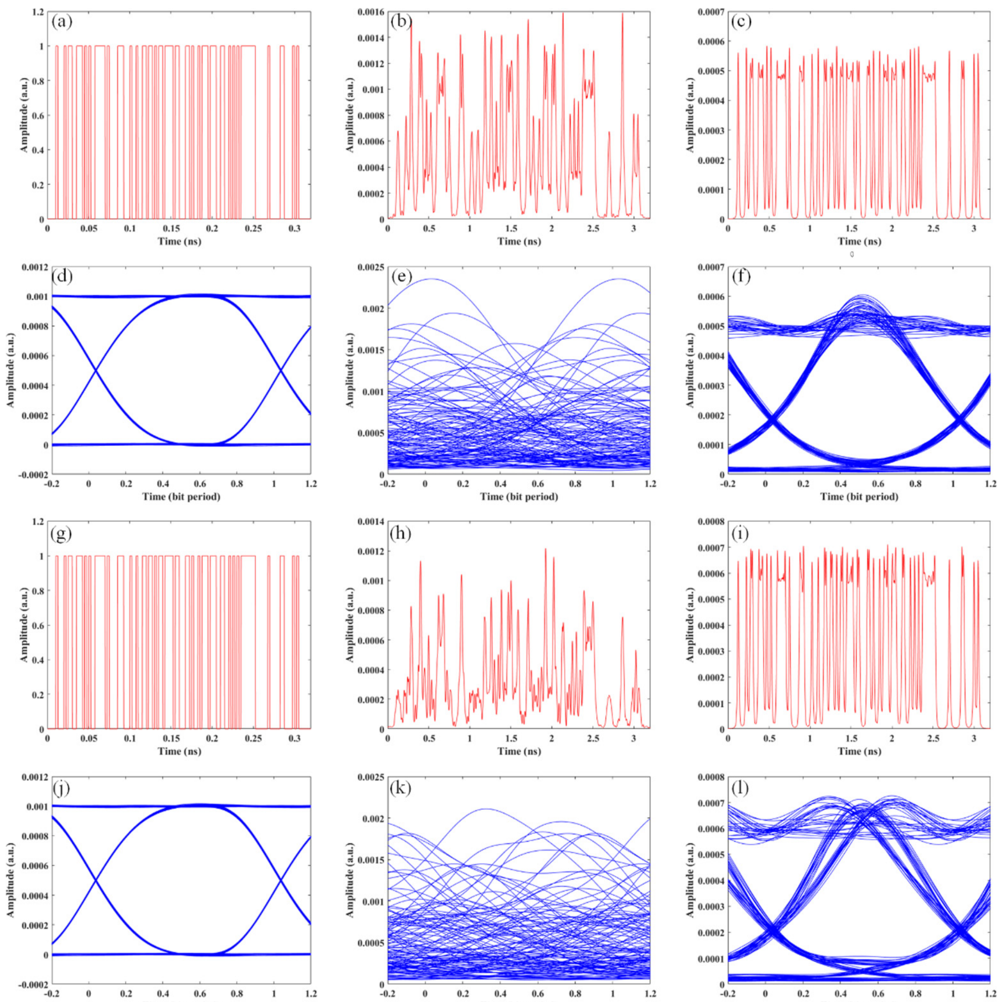


**Fig. 13.** Dispersion compensation in high-speed optical fiber transmission system: Waveform of (a) original signal, (b) before dispersion compensation, and (c) after dispersion compensation at 1550.04 nm. Eye diagram of (d) the original signal, (e) before dispersion compensation, and (f) after dispersion compensation at 1550.04 nm. Waveform of (g) original signal, (h) before dispersion compensation, and (i) after dispersion compensation at 1545.12 nm. Eye diagram of (j) the original signal, (k) before dispersion compensation, and (l) after dispersion compensation at 1545.12 nm.

of the structure designed in this work. Meanwhile, for the structures suggested in [22–24], not only do they have large ILs and small dispersion values, but also the device sizes are relatively large. Compared with them, the cascaded nested MRR dispersion compensator proposed here has excellent advantages in both dispersion value and device size.

**Table 1. Performance comparison of on-chip dispersion compensators**

| Ref | Type | Material | Dispersion (ps/nm) | Insertion loss (dB) | Size | Physical device/ simulations |
|---|---|---|---|---|---|---|
| [22] | WBG | SOI | +250 @1540nm | 3 | 1cm | physical device |
| [23] | WBG | SOI | +20 @1270nm | 4 | 8.5mm | physical device |
| | | | -28 @1335nm | | | |
| [24] | CWMG | TFLN | -39.3@1550nm | 6 | 0.16mm × 4.65mm | physical device |
| [38] | MRR | SiON | -4000@1550nm | 3 | 2.5 mm × 2.5 mm | physical device |
| [39] | MRR | $Si_3N_4$ | $-12.3\times10^3$ @1550nm | 0.1 | 100µm × 100µm | physical device |
| [52] | WBG | SOI | -11@1570nm | 2 | 4µm × 3.72mm | simulations |
| [53] | MRR | ~ | $-3.6\times10^3$@1550nm | 3 | ~ | simulations |
| [54] | MRR | ~ | -3993@1550nm | 19 | ~ | simulations |
| This Work | MRR | SOI | $-34.6\times10^3$ @1550nm | 0.44 | 25µm × 27µm | simulation |
| | | | -7567.1@1545nm | | | |

## 4. Conclusion

A novel dual-channel dispersion compensator with ultra-compactness based on SOI is proposed. By cascading two sets of nested MRR with different sizes, the dispersion compensator achieves large group delay and extremely high negative dispersion at two distinct wavelengths, thereby enabling dual-channel dispersion compensation. The proposed cascading nested MRRs structure is optimized by employing the FDTD method, and its group delay and chromatic dispersion characteristics are analyzed. The results indicate that when the structure parameters are set as $W = 600$ nm, $H = 220$ nm, $R_1 = 6.716$ µm, $R_2 = 4.795$ µm, $R_3 = 4.802$ µm, $R_4 = 3$ µm, $g = 0.1$ µm, and $G = 10$ µm, the maximum group delay of 266.41 ps and the largest negative dispersion of -34611.6 ps/nm can be attained at 1550 nm. Meanwhile, at 1545 nm, the maximum values of the group delay and negative dispersion are -112.13 ps and -7567.1 ps/nm respectively. Moreover, the device size is only 25 µm × 27 µm, and the IL is less than 0.44 dB. In addition, the device is utilized for dispersion compensation of a 40 Gbit/s NRZ signal transmitted through 100 km of SMF. The results reveal that after dispersion compensation, the Q factor of the 1550.04 nm signal is 7.71 with a minimum BER of $10^{-15}$. The Q factor of the 1545.12 nm signal is 7.18 with a minimum bit error rate of $10^{-13}$. All these validate the efficacy of the dispersion compensator. The proposed cascaded nested MRR dispersion compensator features higher dispersion and compact size, showing great application potential in high-speed optical transceiver chips as well as large-scale PICs.

**Funding.** National Key Research and Development Program of China (2022YFB2903201); National Natural Science Foundation of China (62105260); Shaanxi Provincial Department of Education Collaborative Innovation Project (20JY060).

**Disclosures.** The authors declare no conflicts of interest.

**Data availability.** Data underlying the results presented in this paper are not publicly available at this time but may be obtained from the authors upon reasonable request.

### References

1. Q. Hu, M. Chagnon, K. Schuh, *et al.*, "IM/DD beyond bandwidth limitation for data center optical interconnects," J. Lightwave Technol. **37**(19), 4940–4946 (2019).

2. A. Uchiyama, S. Okuda, Y. Hokama, *et al.*, "225 Gb/s PAM4 2 km and 10 km transmission of electro-absorption modulator integrated laser with hybrid waveguide structure for 800 Gb/s and 1.6 Tb/s transceivers," J. Lightwave Technol. **42**(4), 1225–1230 (2024).
3. A. S. Karar, "Iterative algorithm for electronic dispersion compensation in IM/DD systems," J. Lightwave Technol. **38**(4), 698–704 (2020).
4. L. Grüner-Nielsen, M. Wandel, P. Kristensen, *et al.*, "Dispersion-compensating fibers," J. Lightwave Technol. **23**(11), 3566–3579 (2005).
5. K. O. Hill, F. Bilodeau, B. Malo, *et al.*, "Chirped in-fiber Bragg gratings for compensation of optical-fiber dispersion," Opt. Lett. **19**(17), 1314–1316 (1994).
6. Y. Han and S. B. Lee, "Tunable dispersion compensator based on uniform fiber Bragg grating and its application to tunable pulse repetition-rate multiplication," Opt. Express **13**(23), 9224–9229 (2005).
7. D. Zou, F. Li, W. Wang, *et al.*, "Modified gerchberg-saxton algorithm based electrical dispersion pre-compensation for intensity-modulation and direct-detection systems," J. Lightwave Technol. **40**(9), 2840–2849 (2022).
8. A. S. Karar, "Gerchberg-Saxton based FIR filter for electronic dispersion compensation in IM/DD transmission Part I: Theory and simulation," J. Lightwave Technol. **41**(5), 1335–1345 (2023).
9. G. F. Chen, K. Y. Ong, and D. T. Tan, "Chip-Scale Dispersion Compensation of High-Speed Data–Recent Progress and Future Perspectives," Laser & Photonics Rev. **19**(6), 2400755 (2025).
10. S. Y. Siew, B. Li, F. Gao, *et al.*, "Review of silicon photonics technology and platform development," J. Lightwave Technol. **39**(13), 4374–4389 (2021).
11. J. R. Ong, R. Kumar, and S. Mookherjea, "Silicon microring-based wavelength converter with integrated pump and signal suppression," Opt. Lett. **39**(15), 4439–4441 (2014).
12. N. J. Hussein, S. R. Saeed, and A. S. Hatem, "Design of a nano-scale optical 2-bit analog to digital converter based on artificial intelligence," Appl. Opt. **63**(19), 5045–5052 (2024).
13. S. Idres, J. L. Habif, and H. Hashemi, "Universal all-optical zero-bias logic gates in silicon photonics," Opt. Express **32**(21), 36063–36074 (2024).
14. A. L. Gaeta, M. Lipson, and T. J. Kippenberg, "Photonic-chip-based frequency combs," Nat. Photonics **13**(3), 158–169 (2019).
15. J. Wang, F. Sciarrino, A. Laing, *et al.*, "Integrated photonic quantum technologies," Nat. Photonics **14**(5), 273–284 (2020).
16. Z. Zhou, B. Yin, and J. Michel, "On-chip light sources for silicon photonics," Light Sci. Appl. **4**(11), e358 (2015).
17. J. Feldmann, N. Youngblood, M. Karpov, *et al.*, "Parallel convolutional processing using an integrated photonic tensor core," Nature **589**(7840), 52–58 (2021).
18. S. Shekhar, W. Bogaerts, L. Chrostowski, *et al.*, "Roadmapping the next generation of silicon photonics," Nat. Commun. **15**(1), 751 (2024).
19. A. Rickman, "The commercialization of silicon photonics," Nat. Photonics **8**(8), 579–582 (2014).
20. Z. Hui, M. Yang, D. Pan, *et al.*, "Slot–slot waveguide with negative large and flat dispersion covering C+ L+ U waveband for on-chip photonic networks," Appl. Opt. **58**(21), 5728–5739 (2019).
21. K. Takiguchi, "Integrated-optic chromatic dispersion compensator composed of arrayed-waveguide gratings and delay lines," Proc. SPIE **12425**, 1242503 (2023).
22. T. Ma, K. Nallapan, H. Guerboukha, *et al.*, "Analog signal processing in the terahertz communication links using waveguide Bragg gratings: example of dispersion compensation," Opt. Express **25**(10), 11009–11026 (2017).
23. M. Kim, J. Ju, S. K. Park, *et al.*, "Control of linear chirps in waveguide Bragg gratings by applying designed core profiles," J. Lightwave Technol. **27**(21), 4809–4813 (2009).
24. S. Liu, R. Ma, W. Wang, *et al.*, "Ultra-compact thin-film-lithium-niobate photonic chip for dispersion compensation," Nanophotonics **13**(26), 4723–4731 (2024).
25. X. Yuan, K. Liu, W. Ye, *et al.*, "Dispersion compensation based on the combination of coupled ring resonator and photonic crystal structures," Chin. Opt. Lett. **9**(9), 92301–92303 (2011).
26. J. Liu, E. Lucas, A. S. Raja, *et al.*, "Photonic microwave generation in the X- and K-band using integrated soliton microcombs," Nat. Photonics **14**(8), 486–491 (2020).
27. Y. Liu, Y. Chen, L. Wang, *et al.*, "Tunable and reconfigurable microwave photonic bandpass filter based on cascaded silicon microring resonators," J. Lightwave Technol. **40**(14), 4655–4662 (2022).
28. J. Xie, L. Zhou, Z. Zou, *et al.*, "Continuously tunable reflective-type optical delay lines using microring resonators," Opt. Express **22**(1), 817–823 (2014).
29. J. M. Chavez Boggio, D. Bodenmüller, S. Ahmed, *et al.*, "Efficient Kerr soliton comb generation in micro-resonator with interferometric back-coupling," Nat. Commun. **13**(1), 1292 (2022).
30. R. Wang, P. Wang, C. Lyu, *et al.*, "Photonic binary convolutional neural network based on microring resonator array," IEEE Photonics Technol. Lett. **35**(12), 664–667 (2023).
31. M. Savanier, R. Kumar, and S. Mookherjea, "Photon pair generation from compact silicon microring resonators using microwatt-level pump powers," Opt. Express **24**(4), 3313–3328 (2016).
32. H. Mahmudlu, R. Johanning, A. Rees, *et al.*, "Fully on-chip photonic turnkey quantum source for entangled qubit/qudit state generation," Nat. Photonics **17**(6), 518–524 (2023).
33. R. Haldar, S. Das, and S. K. Varshney, "Theory and design of off-axis microring resonators for high-density on-chip photonic applications," J. Lightwave Technol. **31**(24), 3976–3986 (2013).

34. R. Haldar, A. D. Banik, and S. K. Varshney, "Design of CMOS compatible and compact, thermally-compensated electro-optic modulator based on off-axis microring resonator for dense wavelength division multiplexing applications," Opt. Express **22**(19), 22411–22420 (2014).
35. M. C. M. M. Souza, G. F. M. Rezende, L. A. Barea, *et al.*, "Modeling quasi-dark states with temporal coupled-mode theory," Opt. Express **24**(17), 18960–18972 (2016).
36. R. Haldar, S. Ummethala, R. K. Sinha, *et al.*, "Nested nonconcentric microring resonators with high-Q and large fabrication tolerance," J. Opt. Soc. Am. B **38**(12), 3743–3753 (2021).
37. V. Sorianello, G. De Angelis, F. Fresi, *et al.*, "100Gb/s PolMux-NRZ Transmission at 1550 nm over 30 km Single Mode Fiber Enabled by a Silicon Photonics Optical Dispersion Compensator," in *Optical Fiber Communication Conference* (Optica Publishing Group, 2018).
38. Y. Liu, L. Lu, Z. Ni, *et al.*, "Silicon Integrated Continuously Tunable Dispersion Compensator Based on Cascaded Micro-Ring Resonators," in *Asia Communications and Photonics Conference* (IEEE, 2022).
39. K. Y. K. Ong, G. F. R. Chen, P. Xing, *et al.*, "Dispersion compensation of high-speed data using an integrated silicon nitride ring resonator," Opt. Express **30**(9), 13959–13967 (2022).
40. L. Zhang, A. M. Agarwal, L. C. Kimerling, *et al.*, "Nonlinear Group IV photonics based on silicon and germanium: from near-infrared to mid-infrared," Nanophotonics **3**(4-5), 247–268 (2014).
41. H. Takahashi, R. Inohara, K. Nishimura, *et al.*, "Expansion of bandwidth of tunable dispersion compensator based on ring resonators utilizing negative group delay," J. Lightwave Technol. **24**(6), 2276–2286 (2006).
42. L. Zhang, M. Song, J.-Y. Yang, *et al.*, "A compact chromatic dispersion compensator using unequal and mutually-coupled microring resonators," *Integrated Photonics and Nanophotonics Research and Applications* (2008).
43. W. Bogaerts, P. De Heyn, T. Van Vaerenbergh, *et al.*, "Silicon microring resonators," Laser & Photonics Rev. **6**(1), 47–73 (2012).
44. K. D. Ferris, "Fiber-optic communication link for missile guidance," *Optical Fiber Communication Conference*, TUE2 (1981).
45. Y. Fu, M. Cheng, X. Jiang, *et al.*, "High-speed optical secure communication with an external noise source and an internal time-delayed feedback loop," Photonics Res. **7**(11), 1306–1313 (2019).
46. G. Pandey, A. Choudhary, and A. Dixit, "Wavelength division multiplexed radio over fiber links for 5 G fronthaul networks," IEEE J. Select. Areas Commun. **39**(9), 2789–2803 (2021).
47. R. Bhattacharjee, P. Dey, and A. Sah, "An improved hybrid OTDM-WDM transmission system for effective nonlinearity mitigation utilizing Ti:PPLN waveguide based OPC module," Optik **219**, 165241 (2020).
48. H. Y. Ahmed, M. Zeghid, W. A. Imtiaz, *et al.*, "Adaptive transceiver architecture with QoS provision for OCDMA network based on logic gates," IEEE Access **9**(3), 151089–151109 (2021).
49. Y. Li, C. Wu, P. He, *et al.*, "Modeling of nonlinear interference in the same- wavelength bidirectional coherent fiber communication systems," IEEE Photonics J. **15**(5), 1–9 (2023).
50. Y. Ding, X. Zhu, S. Xiao, *et al.*, "Effective electro-optical modulation with high extinction ratio by a graphene–silicon microring resonator," Nano Lett. **15**(7), 4393–4400 (2015).
51. X. Liu, P. Ying, X. Zhong, *et al.*, "Highly efficient thermo-optic tunable micro-ring resonator based on an LNOI platform," Opt. Lett. **45**(22), 6318–6321 (2020).
52. W. Shi, V. Veerasubramanian, D. Patel, *et al.*, "Tunable nanophotonic delay lines using linearly chirped contradirectional couplers with uniform Bragg gratings," Opt. Lett. **39**(3), 701–703 (2014).
53. J. Montalvo and C. Vázquez, "Ring resonator with an internal Sagnac loop for dispersion compensation in DWDM backbone networks," Proc. SPIE **6593**, 65931E (2007).
54. B. B. Bhowmik, S. Gupta, and R. Gangopadhyay, "Simultaneous demodulation and dispersion compensation of WDM DPSK channels using optical ring resonator," Opt. Commun. **285**(16), 3483–3486 (2012).